HHS Public Access

Author manuscript

Nat Med. Author manuscript; available in PMC 2015 January 01.

Published in final edited form as:

Nat Med. 2014 July ; 20(7): 785–789. doi:10.1038/nm.3590.

Noninvasive two-photon fluorescence microscopy imaging of mouse retina and RPE through the pupil of the eye

Grazyna Palczewska[1], **Zhiqian Dong**[1], **Marcin Golczak**[2], **Jennifer J. Hunter**[3,4], **David R. Williams**[3,5], **Nathan S. Alexander**[2], and **Krzysztof Palczewski**[1,2]

[1]Polgenix Inc., Cleveland, Ohio 44106, USA

[2]Department of Pharmacology, Case Western Reserve University, Cleveland, Ohio, USA

[3]Center for Visual Science, Flaume Eye Institute, University of Rochester, Rochester, New York, USA

[4]Biomedical Engineering, University of Rochester, Rochester, New York, USA

[5]The Institute of Optics, University of Rochester, Rochester, New York, USA

Abstract

Two-photon excitation microscopy (TPM) can image retinal molecular processes *in vivo*. Intrinsically fluorescent retinyl esters in sub-cellular structures called retinosomes are an integral part of the visual chromophore regeneration pathway. Fluorescent condensation products of all–*trans*–retinal accumulate in the eye with age and are also associated with age-related macular degeneration (AMD). Here we report repetitive, dynamic imaging of these compounds in live mice, through the pupil of the eye. Leveraging advanced adaptive optics we developed a data acquisition algorithm that permitted the identification of retinosomes and condensation products in the retinal pigment epithelium (RPE) by their characteristic localization, spectral properties, and absence in genetically modified or drug-treated mice. This imaging approach has the potential to detect early molecular changes in retinoid metabolism that trigger light and AMD-induced retinal defects and to assess the effectiveness of treatments for these conditions.

Noninvasive imaging of biochemical processes at subcellular resolution *in vivo* represents a new frontier in discovering the details of biological processes and the impact of disease and therapies. Two-photon excitation microscopy (TPM) based on two-photon excitation (2PE) fluorescence imaging can achieve this goal by employing infrared excitation light that non–destructively penetrates deep into tissues [1].

A 2PE is well-suited for retinal imaging because the sclera, cornea and lens are highly transparent to infrared light [2-5]. The 2PE rate is proportional to the square of incident light

Author Contributions: G.P. and K.P. conceived and directed the project. G.P., M.G., Z.D. and N.S.A., designed and conducted experiments and generated software. G.P., N.S.A. and K.P. prepared the manuscript. J.J.H. and D.R.W. edited the manuscript.

Competing Financial Interests: G.P. and Z.D. are employees of Polgenix. K.P. is CSO at Polgenix Inc. K.P. is an inventor of the U.S. Patent No. 7,706,863 and U.S. Patent No. 8,346,345 whose value may be affected by this publication. N.S.A and M.G., report no conflict of interest. The J.J.H and D.R.W. laboratories received support from Polgenix Inc.

intensity [6]. Therefore using adaptive optics to correct for wavefront errors introduced by the lens and cornea [7-10] improves resolution and maximizes the 2PE rate [11], by achieving a tightly focused excitation beam. However, the two-photon absorption cross sections of native fluorophores are small (on the order of 10^{-52} cm^4 s per photon [12]), which necessitates improvements in 2PE imaging efficiency. The number of photons generated by 2PE is inversely proportional to the laser pulse duration [6], so application of lasers delivering pulses shorter than 75 fs, coupled with correction for group delay dispersion can more than double 2PE-induced fluorescence [13]. Further improvements come from highly sensitive/low noise detectors with thermoelectric cooling, and the application of sophisticated software algorithms for image acquisition and analysis. With these advances, biochemical processes in the RPE and the neuronal cells can be monitored [5].

The fluorophore content of the retina–RPE region reflects the efficiency of the visual cycle, (i.e. visual chromophore, 11–*cis*–retinal, regeneration), and changes in response to external stress, genetic manipulations and treatments [14-16]. Retinoids are intrinsic fluorophores with absorption spectra that respond to 2PE [3,4]. During ageing, retinal retinoids form condensation products, such as A2E that are also fluorescent [17], and detectable by TPM, and are biomarkers for potentially toxic retinoids that form early in degenerative retinopathies such as Stargardt disease and age-related macular degeneration (AMD) [5,18].

The challenge now is to develop TPM instrumentation[7] that can safely and periodically image the retina and RPE to detect and follow abnormalities in biochemical transformations well before electrophysiological and pathological changes become evident. Here, we present the first fundamental step towards this goal.

Results

RPE imaging through a mouse eye pupil

To image the RPE and retina in live mice we assembled an instrument containing a 75 fs laser with integrated group delay dispersion pre-compensation, adaptive optics modulating the excitation light and a fluorescence detector in a non-descanned configuration (Fig. 1a). Initial images of RPE created by endogenous fluorophores were obtained with *ex vivo* mouse eyes submerged in phosphate-buffered saline solution and a deformable mirror (DM) set to a neutral position (Fig. 1 a, b, c). We optimized dispersion pre-compensation, which increased the mean fluorescence an average of 5-fold (Fig. 1d), indicating that in the RPE, 75 fs laser pulses would elongate to 400 fs [6]. Iterative changes of the DM surface shape (Fig. 1e), resulted in further increased mean fluorescence from 34.6 to 58.1 in arbitrary units and increased dynamic range of the images, quantified as the range of pixel values, from 176 to 237 with 255 being the maximum (Fig. 1f).

To assess the capabilities of our system to characterize the RPE and retina we imaged *ex vivo* eyes of mice with different genetic backgrounds. The brightest RPE images were obtained in *Rpe65*$^{-/-}$ mice in response to 730 nm excitation (Fig. 2a). The brightly fluorescent granules correspond to enlarged retinosomes, which are a characteristic feature of the RPE only in *Rpe65*$^{-/-}$ mice due to blockade of 11–*cis*–retinol synthesis [3,5,19]. Double nuclei and retinosomes located close to individual cell membranes were also resolved (Fig.

2a). In contrast to *Rpe65*$^{-/-}$ mice, predominant fluorophores in the RPE of *Abca4*$^{-/-}$*Rdh8*$^{-/-}$ (DKO) mice were retinal condensation products [5]. Fluorophores in these mice were more visible with an 850 nm excitation and were uniformly distributed within the RPE cell, so the black nuclei, free of fluorophores, were defined in TPM images (Fig. 2b). Retinosomes were visible in wild type (WT) mice exposed to white light for 30 min at 5,000 lux before imaging (Fig. 2c), and more clearly visible in WT mice pre-treated with retinylamine (Ret–NH_2), a powerful inhibitor of the retinoid cycle [20], even though the laser power was reduced by 17% for the same detector settings (Supplementary Fig. 1). We also imaged and counted the neuronal nuclei in the ganglion cell layer at 0.6 mm eccentricity and found 2,500 nuclei per mm^2 (Fig. 2d), which is smaller than previously reported ∼7,000 per mm^2 of combined ganglion and displaced amacrine cells [21] in stained retina. This difference arises from: a) nuclei are free of fluorophores, and are only visible as dark structures against brighter cell bodies, which can lead to obstruction of the nuclei by axon bundles [22,23]; b) not all the cell nuclei were at the same imaging depth; and c) the estimates of the area could be off by 40% because they were determined by comparing measurements of optic disk in *en face* TPM images to histological sections. Not all the cell nuclei were at the same location along the optical axis [24], the difference by only half of a ganglion cell soma diameter would place some of the somas out of TPM focus, because: a) the range of retinal ganglion cells somas diameters is 7-30 μm [25]; b) the theoretical optical resolution along optical axis, estimated following Zipffel *et al* [26] was ∼4.5 μm; and c) different layers of the retina come in and out of focus (Supplementary Video 1). Despite variances in absolute values of ganglion cell density, TPM-based visualization provides a non-invasive method for verification of the health of ganglion cell layer [10].

Evaluation of drug therapy on RPE preservation

Ret–NH_2 protects mouse RPE and retina from deterioration caused by prolonged exposure to bright light [18]. Using 2PE trans-pupil imaging *ex vivo*, 7 and 14 days after bright light exposure we found an over-accumulation of fluorescent granules in the RPE of untreated control DKO mice but no deposits in mice treated with Ret–NH_2 (Fig. 3a). These granules were more clearly visible when imaged with 850 nm rather than 730 nm light, indicating that they were condensation products of all–*trans*–retinal. Before we measured their emission spectra, we performed trans-pupil imaging of the retina of *hrhoG/hrhoG* mice (Fig. 3b) and determined that its emission maximum was at 512 nm [27]. The spectra were almost identical with those obtained through the sclera (Supplementary Fig. 2) and the previously published maximum at 511 nm [28]. Emission spectrum from granules in DKO mice had maximum at 628 nm. Even though slightly red–shifted, it is comparable with previous reports [17], confirming their origin as all–*trans*–retinal condensation products (Fig. 3c). Emission spectra obtained through the sclera showed a higher contribution of fluorophores emitting at shorter wavelengths, in agreement with brighter images obtained with 730 nm (Fig. 3a) as compared to trans-pupil, possibly caused by the spectral filtering introduced by the retina or anterior optics.

We counted the fluorescent granules; there were no differences in the quantity of fluorescent granules 7 days and 14 days after bleaching (Fig. 3d). Double nuclei and RPE cell borders are visible in the bottom panel of Fig 3e.

Localization of bright fluorescent granules

Using a z-axis translation stage in our *in vivo* imaging system (Fig. 4a), we determined that the fluorescent granules responding to 850 nm excitation in live pigmented DKO mice exposed to bright light were located 3.0 mm away from the cornea (Fig 4b). With 730 nm excitation we imaged retinosomes in live *Rpe65*$^{-/-}$ mice 3.2 mm posterior to the cornea; differences likely result from mouse to mouse random variations [29]. No fluorescence was observed in these mice using 850 nm light (Fig. 4c) [5,30]. The spectrum from the RPE of *Rpe65*$^{-/-}$ mice was obtained with 730 nm and revealed maxima at 480 nm, 511 nm and a shoulder at 463 nm, whereas the spectrum from DKO mice was obtained with 850 nm and was shifted to longer wavelengths (Fig. 4d). The emission maxima at both 480 nm and 511 nm are likely generated by retinyl esters [5,31], whereas the shoulder at 463 nm is probably due to NADPH [32]. The maximum around 511 nm could also be derived from all–*trans*–retinal [33], but the abundance of retinyl esters in *Rpe65*$^{-/-}$ mice favors these retinoids as the primary source.

We counted on average 536 fluorescent granules per mm^2 (Fig. 4e). The difference between *ex vivo* (Fig. 3d) and *in vivo* (Fig. 4e) was not statistically significant. The uneven edges of the cornea and lens sutures (Fig 4b), corresponding to ∼145 breath/min of the mouse, result from using a slower acquisition rate for this image. Examination of TPM RPE images obtained during DM surface optimization did not indicate damage to RPE (Supplementary Video 2).

Discussion

This work offers several advances over previous reports of TPM imaging of the retina [3,5,7,10]. These include a) the first images of retinoid cycle fluorophores in RPE of living pigmented mammals and their spectral and spatial characterization; b) the first TPM images of rod photoreceptor cells; and c) the characterization of endogenous and artificial fluorophores in retina affected by genetic disorders, environmental stress or drug therapy.

As TPM technology improves, we can expect high resolution images without jeopardizing safety, facilitating its translation into clinical applications. When imaging pigmented animals more noise will occur because of relatively uniform distribution of melanin within the RPE and microvilli. However, melanin fluorescence in response to infra-red light was reported to be 60 to 100 times less than the fluorescence of lipofuscin [34]. Combined with our results in pigmented animals, this makes us optimistic about prospects of using TPM to image the human eye.

TPM can be used to accelerate drug discovery and development by rapidly evaluating how compounds interact with tissues by determining their *in vivo* site(s) of action, as well as treatment safety and efficacy. Together with insights derived from parallel molecular, cellular and pathophysiological studies, TPM can foster effective treatment strategies for retinal diseases such as AMD, Stargardt disease and diabetic retinopathy. The cost effectiveness of using software driven adaptive optics will make TPM an attractive tool as therapeutic research transitions from mice to humans.

Applications of non-endogenous fluorescent proteins will allow monitoring of protein expression, translocation and changes in specific cell types expressing customized protein fluorescent sensors. Such fluorophores could provide the first clues about ensuing pathology for common central nervous system diseases such as multiple sclerosis and Alzheimer disease [35]. 2PE-based imaging of the eye can potentially be used to understand connectivity and function of retinal neurons *in vivo*, including pathological changes such as neovascularization within the retina or brain damage after a stroke.

The applications of multi–photon excitation complement yet far exceed the capabilities of either optical coherence tomography (OCT)[36] or scanning laser ophthalmoscopy (SLO)[37]. OCT cannot visualize fluorophores. TPM can image fluorophores that are accessible to SLO only when using retina-harming UV light [38]. Additionally, the longer excitation wavelengths employed by TPM are less prone to scattering when traveling through the tissue. Specifically, TPM can detect vitamin A metabolites and their toxic by-products, thus making it the best current method to non-destructively monitor disease progression in the same animal.

There is minimal information available regarding retinal damage in mice from laser pulses of less than 100 fs duration. However, considering that it took 4–6 min to achieve an optimal DM shape, and based on previous reports [39], our laser power was almost 10 times higher than safety limits based on thermal continuous-wave calculations for multiple exposures [38]. Nonetheless we did not detect any damage after TPM imaging. Improved detectors and further shortened laser pulses will reduce the laser power required to obtain retinal images [40]. However, extensive safety studies in mice and primates are needed before this technology is employed in humans.

Online Methods

Mice

All animal procedures and experiments were approved by the Institutional Animal Care and Use Committee at Case Western Reserve University and conformed to recommendations of both the American Veterinary Medical Association Panel on Euthanasia and the Association for Research in Vision and Ophthalmology. B6(Cg)-Tyr$^{c\text{-}2J}$/J mice were purchased from The Jackson Laboratory. *Abca4*$^{-/-}$*Rdh8*$^{-/-}$ (DKO) and *Rpe65*$^{-/-}$ mice were generated and genotyped as previously described [5]. Human opsin–GFP fusion, knock–in *hrhoG/hrhoG* mice, expressing human rhodopsin–GFP in photoreceptor outer segments were kindly provided by Dr. John H. Wilson (Baylor College of Medicine) [27]. All mice were housed in the animal facility at the School of Medicine, Case Western Reserve University, where they were provided with a regular mouse chow diet and maintained either under complete darkness or in a 12 h light (∼10 lux)/12 h dark cyclic environment. Euthanasia was performed in compliance with American Veterinary Medical Association (AVMA) Guidelines on Euthanasia, and approval by the Case Western Reserve University Institutional Animal Care and Use Committee. All mice used in this study were between 1–6-month-old. We used both male and female animals.

DKO mouse pupils were dilated with 1% tropicamide prior to bright white light exposure at 10,000 lux (150 W spiral lamp, Commercial Electric) for 60 min. After bright light exposure animals were housed in the dark until subsequent imaging sessions. Two-photon imaging to assess RPE and retinal changes was performed 7 and 14 days after bright light exposure.

Two–photon imaging was done through mouse eye pupil unless otherwise indicated, and either *in vivo* or with freshly enucleated mouse eyes for *ex vivo* imaging. For in vivo imaging, mice were anesthetized with an intraperitoneal injection of anesthetic solution consisting of ketamine (15 mg/ml), xylazine (3 mg/ml) and acepromazine 0.5 mg/ml diluted with water at a dose of 10 μl/g body weight (bw).

To enhance the visibility of retinosomes, WT mice without any drug treatment or treated with Ret–NH_2 were exposed to 5,000 lux of white light for 5–30 min, 1 to 3 h before imaging.

OCT

OCT imaging to verify retina integrity after TPM imaging was performed using SD-OCT Envisu R2200 (Bioptigen, Morrisville, NC)

Retinylamine treatment

Ret–NH_2 was synthesized as described previously [20]. Mice (4– to 6-week-old) were gavaged with 2 mg of Ret–NH_2 solubilized in 100 μl soybean oil 13 to 16 h prior to bright light exposure. Two-photon imaging was performed 7 and 14 days after bright light exposure.

After treatment with Ret–NH_2 the content of fluorescent retinyl esters increases in the eye as reported previously [20,41]. However, 7 days after treatment that increase has already diminished [42]. For quantification of the impact of drug treatment, the same detector settings were used for mice that were treated and not treated with Ret–NH_2. This also applied to imaging with either 730 nm or 850 nm excitation. To prevent overload of the detector in this experiment, the settings were optimized to visualize condensation products (not retinyl esters), which were abundant in animals that were not treated with Ret–NH_2. This is why outlines of RPE cell borders are only very slightly visible in animals that were treated with Ret–NH_2.

The fluorescence intensity was brighter 14 days after light exposure than 7 days after exposure because it took some time for RPE cells to accumulate condensation products resulting from light exposure in mice that were not treated with Ret–NH_2.

Two–photon imaging system for mouse retina and RPE

To achieve 2PE images of the retina and RPE with laser light entering through the mouse eye pupil, we modified the Leica (Wetzlar, Germany) TCS SP5 to include: an upright DM600 microscope stand, a Chameleon Vision–S (Coherent, Santa Clara, CA) femtosecond laser, an objective with a 0.5 numerical aperture and 15 mm working distance, and a custom adaptive optics system including a deformable mirror (DM) (see Fig. 1a, 1b).

The tunable, 690–1050 nm, Chameleon Vision–S generated 75 fs laser pulses at 80 MHz pulse repetition frequency. To minimize laser pulse duration at the sample, the laser was equipped with a group velocity dispersion pre–compensation (DC) unit with a 0 to 43,000 fs^2 range. Laser beam power was controlled with an electro–optic modulator (EOM) contained within a safety box. After the EOM, the laser beam was directed to the adaptive optics component, namely DM, by the fold mirror on a kinematic magnetic base (FMK1). The laser beam was coupled to the DM with expander lenses L1 and L2 (Fig. 1c). A micro-electro-mechanical system DM (Boston Micromachines Corp., Cambridge MA) with 140 actuators, a 5.5 μm stroke, and gold coating provided fine focus adjustment and correction of aberrations introduced by the sample. In two–photon imaging, the excitation matters most because the emission fluorescence is generated only in the focal spot; therefore, it is critical to achieve a tightly focused excitation beam. Only the excitation light was modulated by the DM, which shape was controlled with software based on image quality metric feedback without the use of a wavefront sensor and associated components [7,39,43]. This design reduced the cost of the system and its footprint. Lenses L3 and L4 reduced the size of the beam which, after reflecting off the second fold mirror on a kinematic magnetic base (FMK2), was directed to the scan mirrors. The scan mirrors which operated with typical line frequency of 400 to 700 Hz and 512 to 1024 lines per frame, and typical pixel dwell time of 1.46 μs, were located at the plane conjugate to the back aperture of the 0.5 numerical aperture (NA) objective. In this configuration, the laser beam overfilled the mouse eye to take advantage of the NA of the dilated pupil. Laser power entering mouse pupil was 7.4 mW, based on an estimated 3.2 mm laser beam diameter and a 2 mm mouse eye pupil. We verified that estimate by placing a 2 mm iris at a location corresponding to the mouse eye pupil and measuring 8.5 mW using a laser power meter. Additionally, we measured that the needed laser light levels could be cut by over 25%. Only 6.3 mW of laser power was needed for imaging with this HYD detector, as compared to 8.5 mW of laser power required to obtain TPM images with the PMT detector. This represents over a 25% reduction in required laser power. This reduction is consistent with the HYD detector's higher quantum yield. At 500 nm, the quantum yield of the HYD detector was ∼ 45 % as compared to the 27 % quantum yield of the PMT R6357 detector used throughout the study, (Supplementary Fig. 3). The fluorescence detector was located as close to the sample as possible to minimize loss of light available for image formation. Two–photon excited fluorescence leaving mouse eye pupil was collected by the same 0.5 NA lens, and directed to the photomultiplier tube (PMT) detector, Hamamatsu R6357, in a non–descanned manner after the excitation light was reflected off the dichroic mirror (DCh) and filtered by the 680SPET Leica filter. 2PE spectra were obtained with a spectrally sensitive detector in a descanned configuration. For *ex vivo* imaging, the mouse eye was submerged in phosphate–buffered saline composed of 9.5 mM sodium phosphate, 137 mM NaCl and 2.7 mM KCl, and pH 7.4, with the pupil facing the excitation laser beam. For *in vivo* mouse imaging, the animal was surrounded by a heating pad and placed on a mechanical stage, which provided controlled movement around two rotational and in three translational axes (Bioptigen, Morrisville, NC). The mouse eye was covered with GenTeal gel that provided lubrication and refractive index matching with the RGP hard contact lens with a refractive index of 1.46, a radius of 1.7 mm and a flat front surface (Cantor and Nissel, Northamptonshire, UK). This contact lens directed laser light into the mouse eye, compensated for the refractive power of the cornea–air interface,

minimized the impact of corneal deformities and protected cornea from drying during the imaging session.

No changes to the cornea and lens were detectable using a low magnification sectioning microscope after completion of the imaging. Additionally, four weeks after TPM imaging of *Rpe65*$^{-/-}$ mice, we used OCT to check for integrity of retinal layers. No differences were noted between mice that were imaged with TPM and control age–matched *Rpe65*$^{-/-}$ mice that were not imaged. Specifically, the outer nuclear layer average thickness in mice imaged with TPM was equal to 0.040 mm, with standard deviation of 0.002 mm, whereas corresponding measurements in control mice that were not imaged with TPM were 0.037 mm and 0.004 mm (Supplementary Fig. 4).

The scale bars displayed in the images were estimated by comparing measurements of *en face* TPM images of optic disks and histological sections.

LAS AF Leica software and raw image data were used for quantification of fluorescent granules and fluorescence. Granules were counted in the inferior/central portion of the retina. The area selected was about 100 μm away from the edge of the optic disc. The RPE sampling area was kept between 0.05 mm^2 to 0.1 mm^2 for each eye. An example of the distribution of fluorescent granules around the optic disc is shown in Fig. 3e.

To calculate resolution along the optical axis (z-axis) as described in results referring to Fig. 2d, we used 730 nm excitation, the numerical aperture (NA) of the mouse eye equal to 0.4 and the coefficient of refraction of the vitreous humor equal to 1.33 [44].

Image acquisition algorithm

After focusing on the mouse RPE with a mechanical stage, optimization of the DM surface provided fine adjustments of focus and the excitation wavefront. Six Zernike modes were used as the set of basis functions for deformation of the DM surface. Zernike modes are a set of polynomials that are orthogonal to one another and frequently used to describe ophthalmic aberrations [45]. The six modes used were Z_2^0, Z_2^2, Z_2^2, $Z_3^1 Z_3^1$, Z_4^0 [45]. The aberration compensation, ϕ, provided by the DM was $\Phi=\Sigma a_j Z_j$, where Z_j is the Zernike mode with index j and the coefficient a_j is the contribution of Z_j. The coefficients were constrained such that $-1.0<a_j<1.0$. The goal of optimizing the DM surface was to find a set of α coefficients which maximize the quality metric of a collected image. The quality metric used here was the normalized variance of the image [46].

Optimization was performed by one of two procedures. In the first, the six Zernike modes were sequentially optimized. Starting with focus, Z_2^0, the coefficient, a_4 was varied from −0.9 to 0.72 in steps of 0.18 and the normalized variance was calculated at each step. The a_4 of the step which provided the best normalized variance value for the collected image was taken as the optimized coefficient for Z_2^0. The $\alpha_4 Z_2^0$ was applied to the initially flat DM surface, and the procedure was repeated for the other aberration terms (Z_2^2, Z_2^{-2}, $Z_3^1 Z_3^{-1}$, Z_4^0) such that the optimized Zernike modes accumulated on the DM surface. In the end, the vector of a_j had been determined and the mirror had accumulated the corresponding surface

shape. This procedure was applied to image the *hrhoG/hrhoG* mice. The set of such established coefficients was: 0.72, −0.18, 0.00, 0.00, 0.18 and 0.00 for Zernike modes as listed above. The normalized variance of the image taken with these coefficients was 1717 versus the image collected with a flat mirror which had a normalized variance value of 246. This process collected 60 images and took 4–6 min to complete. However, the image with the best normalized variance value was not the image collected with the coefficients determined by the end of the process. The individual rod cells in *hrhoG/hrhoG* mice are difficult to distinguish initially without DM correction because of their small features. Sequential optimization was used to image *hrhoG/hrhoG* mice because each step is more independent of the previous one than in the second method described below. During sequential optimization, there is dependence on the previous steps because each subsequent Zernike mode builds off of the previous optimized Zernike mode. However, in the worst case, this would still provide at minimum 10 images with varying coefficients for defocus from which to choose. Here, the image with the best normalized variance (Fig. 3b) was collected during the defocus optimization stage, providing coefficients of −0.72, 0.00, 0.00, 0.00, 0.00, 0.00 and a normalized variance value of 1943. One possible reason why the image resulting from the complete sequential optimization was not the best in this case could be due to changes in the mouse eye itself, because this optimization was performed on a euthanized mouse. The second procedure for DM optimization is based on the stochastic parallel gradient descent (SPGD) method previously described [47]. The normalized variance value, *V*, was calculated for an image collected using an initial set of a coefficients, specifically, all a_j=0, which corresponds to a flat DM. Next, all a_j were perturbed by a small amount, ζ_j, randomly chosen from between −0.05 and 0.05 in steps of 0.025, but excluding 0.0. This provided a new set of coefficients, $a_j + \zeta_j$. Using the new coefficients, a second image was collected, and the normalized variance was calculated to get V_ζ. Starting coefficients for the next iteration (*i*) were then calculated as $\alpha_j^{i+1}=\alpha_j - \eta\zeta_j(V_\zeta - V)$, where η is the learning rate. Here a value of −0.01 was used for η, which is negative because the normalized variance was being maximized. The iterative process was performed for 40 steps and the DM surface that provided the largest normalized variance value was taken as optimal. This procedure was used to image live *Rpe65*$^{-/-}$ mice (images shown in Fig. 4c). The optimization improved the normalized variance of 2374 for a flat DM to a value of 3024 for an optimized DM surface. The optimized coefficients for this mouse were −0.48, 0.05, 0.28, −0.08, −0.06, −0.24.

The sequential and SPGD optimization methods offer complementary approaches for improving image quality. The sequential optimization performs a search over a broad range of Zernike mode coefficients, which is useful if there are large aberrations or cells will be difficult to distinguish. If the features of interest are not resolved initially after sample preparation, the gradients needed by SPGD may be difficult to determine, but sequential optimization will systematically search and find coefficients that improve image quality. However, for sequential optimization, the search is coarse and the coefficients are not simultaneously optimized, in order to allow broad sampling within a reasonable time-frame. The SPGD performs gradient based optimization simultaneously for all Zernike modes. If the desired features can be resolved after initially localizing and focusing the sample, SPGD could more precisely determine the optimal coefficients compared to sequential

optimization. However, SPGD requires the collection of more images, and therefore requires more time than sequential optimization. Therefore, based on the preparation and initial setup of the sample, one can decide whether SPGD or sequential optimization will be more appropriate, since eyes and aberrations differ greatly even within mice of the same genetic make-up.

Statistical analyses

Data in the bar graphs are expressed as the mean ±S.D. The statistical analyses were carried out with ANOVA. Differences with P values > 0.05 were considered not statistically significant.

Supplementary Material

Refer to Web version on PubMed Central for supplementary material.

Acknowledgments

We thank M. Redmond (National Eye Institute of the US National Institutes of Health) for *Rpe65*$^{-/-}$ mice and J. Wilson (Baylor College of Medicine) for GFP–rhodopsin mice. We also thank Bioptigen for advice on mice preparation for live animal imaging, D. Piston for stimulating discussion and L.T. Webster Jr. and members of Palczewski's laboratory and Polgenix's team for critical comments on the manuscript. Research reported in this publication was supported by the National Eye Institute of the US National Institutes of Health under award numbers R01EY008061, R01EY009339, R24EY021126, P30EY11373 and by the National Institute on Aging of the US National Institutes of Health under award number R44AG043645. N.S.A was supported by National Institutes of Health institutional training grants 5T32EY007157 and 5T32DK007319.

References

1. Helmchen F, Denk W. Deep tissue two-photon microscopy. Nat Methods. 2005; 2:932–940. [PubMed: 16299478]
2. Boettner EA, Wolter JR. Transmission of the oculer media. Invest Ophthalmol Vis Sci. 1962; 1:776–183.
3. Imanishi Y, Batten ML, Piston DW, Baehr W, Palczewski K. Noninvasive two-photon imaging reveals retinyl ester storage structures in the eye. J Cell Biol. 2004; 164:373–383. [PubMed: 14745001]
4. Imanishi Y, Gerke V, Palczewski K. Retinosomes: new insights into intracellular managing of hydrophobic substances in lipid bodies. J Cell Biol. 2004; 166:447–453. [PubMed: 15314061]
5. Palczewska G, et al. Noninvasive multiphoton fluorescence microscopy resolves retinol and retinal condensation products in mouse eyes. Nat Med. 2010; 16:1444–1449. [PubMed: 21076393]
6. Denk W, Strickler JH, Webb WW. Two-photon laser scanning fluorescence microscopy. Science. 1990; 248:73–76. [PubMed: 2321027]
7. Hunter JJ, et al. Images of photoreceptors in living primate eyes using adaptive optics two-photon ophthalmoscopy. Biomed Opt Express. 2010; 2:139–148. [PubMed: 21326644]
8. Godara P, Dubis AM, Roorda A, Duncan JL, Carroll J. Adaptive optics retinal imaging: emerging clinical applications. Optom Vis Sci. 2010; 87:930–941. [PubMed: 21057346]
9. Liang J, Williams DR, Miller DT. Supernormal vision and high-resolution retinal imaging through adaptive optics. J Opt Soc Am A Opt Image Sci Vis. 1997; 14:2884–2892. [PubMed: 9379246]
10. Sharma R, et al. In vivo two-photon imaging of the mouse retina. Biomed Opt Express. 2013; 4:1285–1293. [PubMed: 24009992]
11. Rueckel M, Mack-Bucher JA, Denk W. Adaptive wavefront correction in two-photon microscopy using coherence-gated wavefront sensing. Proc Natl Acad Sci U S A. 2006; 103:17137–17142. [PubMed: 17088565]

12. Huang S, Heikal AA, Webb WW. Two-photon fluorescence spectroscopy and microscopy of NAD(P)H and flavoprotein. Biophys J. 2002; 82:2811–2825. [PubMed: 11964266]
13. Padayatti P, Palczewska G, Sun W, Palczewski K, Salom D. Imaging of protein crystals with two-photon microscopy. Biochemistry. 2012; 51:1625–1637. [PubMed: 22324807]
14. Kiser PD, Golczak M, Maeda A, Palczewski K. Key enzymes of the retinoid (visual) cycle in vertebrate retina. Biochim Biophys Acta. 2012; 1821:137–151. [PubMed: 21447403]
15. Palczewski K. Chemistry and biology of vision. J Biol Chem. 2012; 287:1612–1619. [PubMed: 22074921]
16. von Lintig J, Kiser PD, Golczak M, Palczewski K. The biochemical and structural basis for trans-to-cis isomerization of retinoids in the chemistry of vision. Trends Biochem Sci. 2010; 35:400–410. [PubMed: 20188572]
17. Sparrow JR, Wu Y, Kim CY, Zhou J. Phospholipid meets all-trans-retinal: the making of RPE bisretinoids. J Lipid Res. 2010; 51:247–261. [PubMed: 19666736]
18. Maeda A, et al. Primary amines protect against retinal degeneration in mouse models of retinopathies. Nat Chem Biol. 2012; 8:170–178. [PubMed: 22198730]
19. Maeda T, et al. QLT091001, a 9-cis-retinal analog, is well-tolerated by retinas of mice with impaired visual cycles. Invest Ophthalmol Vis Sci. 2013; 54:455–466. [PubMed: 23249702]
20. Golczak M, Kuksa V, Maeda T, Moise AR, Palczewski K. Positively charged retinoids are potent and selective inhibitors of the trans-cis isomerization in the retinoid (visual) cycle. Proc Natl Acad Sci U S A. 2005; 102:8162–8167. [PubMed: 15917330]
21. Lin B, Wang SW, Masland RH. Retinal ganglion cell type, size, and spacing can be specified independent of homotypic dendritic contacts. Neuron. 2004; 43:475–485. [PubMed: 15312647]
22. Euler T, et al. Eyecup scope--optical recordings of light stimulus-evoked fluorescence signals in the retina. Pflugers Arch. 2009; 457:1393–1414. [PubMed: 19023590]
23. Bueno JM, Gualda EJ, Artal P. Adaptive optics multiphoton microscopy to study ex vivo ocular tissues. J Biomed Opt. 2010; 15:066004. [PubMed: 21198178]
24. Helmstaedter M, et al. Connectomic reconstruction of the inner plexiform layer in the mouse retina. Nature. 2013; 500:168–174. [PubMed: 23925239]
25. Sun W, Li N, He S. Large-scale morphological survey of mouse retinal ganglion cells. J Comp Neurol. 2002; 451:115–126. [PubMed: 12209831]
26. Zipfel WR, Williams RM, Webb WW. Nonlinear magic: multiphoton microscopy in the biosciences. Nat Biotechnol. 2003; 21:1369–1377. [PubMed: 14595365]
27. Chan F, Bradley A, Wensel TG, Wilson JH. Knock-in human rhodopsin-GFP fusions as mouse models for human disease and targets for gene therapy. Proc Natl Acad Sci U S A. 2004; 101:9109–9114. [PubMed: 15184660]
28. Spiess E, et al. Two-photon excitation and emission spectra of the green fluorescent protein variants ECFP, EGFP and EYFP. J Microsc. 2005; 217:200–204. [PubMed: 15725123]
29. Schmucker C, Schaeffel F. A paraxial schematic eye model for the growing C57BL/6 mouse. Vision Res. 2004; 44:1857–1867. [PubMed: 15145680]
30. Katz ML, Redmond TM. Effect of Rpe65 knockout on accumulation of lipofuscin fluorophores in the retinal pigment epithelium. Invest Ophthalmol Vis Sci. 2001; 42:3023–3030. [PubMed: 11687551]
31. Drabent R, Bryl K, Smyk B, Ulbrych K. Retinyl palmitate in water environment Journal of Photochemistry and Photobiology B: Biology. 1997; 37:254–260.
32. Chen C, et al. Reduction of all-trans retinal to all-trans retinol in the outer segments of frog and mouse rod photoreceptors. Biophys J. 2005; 88:2278–2287. [PubMed: 15626704]
33. Moroni L, Gellini C, Salvi PR, Schettino V. Fluorescence of all-trans-retinal as a crystal and in a dense solution phase. Journal of Physical Chemistry A. 2000; 104:11063–11069.
34. Keilhauer CN, Delori FC. Near-infrared autofluorescence imaging of the fundus: visualization of ocular melanin. Invest Ophthalmol Vis Sci. 2006; 47:3556–3564. [PubMed: 16877429]
35. London A, Benhar I, Schwartz M. The retina as a window to the brain-from eye research to CNS disorders. Nat Rev Neurol. 2012; 9:44–53. [PubMed: 23165340]

36. Kocaoglu OP, et al. Imaging cone photoreceptors in three dimensions and in time using ultrahigh resolution optical coherence tomography with adaptive optics. Biomed Opt Express. 2011; 2:748–763. [PubMed: 21483600]

37. Carroll J, et al. The effect of cone opsin mutations on retinal structure and the integrity of the photoreceptor mosaic. Invest Ophthalmol Vis Sci. 2012; 53:8006–8015. [PubMed: 23139274]

38. Delori FC, Webb RH, Sliney DH, American National Standards I. Maximum permissible exposures for ocular safety (ANSI 2000), with emphasis on ophthalmic devices. J Opt Soc Am A Opt Image Sci Vis. 2007; 24:1250–1265. [PubMed: 17429471]

39. Geng Y, et al. Adaptive optics retinal imaging in the living mouse eye. Biomed Opt Express. 2012; 3:715–734. [PubMed: 22574260]

40. Xi P, Andegeko Y, Pestov D, Lovozoy VV, Dantus M. Two-photon imaging using adaptive phase compensated ultrashort laser pulses. Journal of Biomedical Optics. 2009; 14

41. Golczak M, et al. Lecithin:retinol acyltransferase is responsible for amidation of retinylamine, a potent inhibitor of the retinoid cycle. J Biol Chem. 2005; 280:42263–42273. [PubMed: 16216874]

42. Maeda A, et al. Effects of potent inhibitors of the retinoid cycle on visual function and photoreceptor protection from light damage in mice. Mol Pharmacol. 2006; 70:1220–1229. [PubMed: 16837623]

43. Zhang Y, Poonja S, Roorda A. MEMS-based adaptive optics scanning laser ophthalmoscopy. Opt Lett. 2006; 31:1268–1270. [PubMed: 16642081]

44. Remtulla S, Hallett PE. A schematic eye for the mouse, and comparisons with the rat. Vision Res. 1985; 25:21–31. [PubMed: 3984214]

45. Thibos LN, et al. Standards for reporting the optical aberrations of eyes. J Refract Surg. 2002; 18:S652–660. [PubMed: 12361175]

46. Sun Y, Duthaler S, Nelson BJ. Autofocusing in computer microscopy: selecting the optimal focus algorithm. Microsc Res Tech. 2004; 65:139–149. [PubMed: 15605419]

47. Vorontsov MA, Sivokon VP. Stochastic parallel-gradient-descent technique for high-resolution wave-front phase-distortion correction. Journal of the Optical Society of America a-Optics Image Science and Vision. 1998; 15:2745–2758.

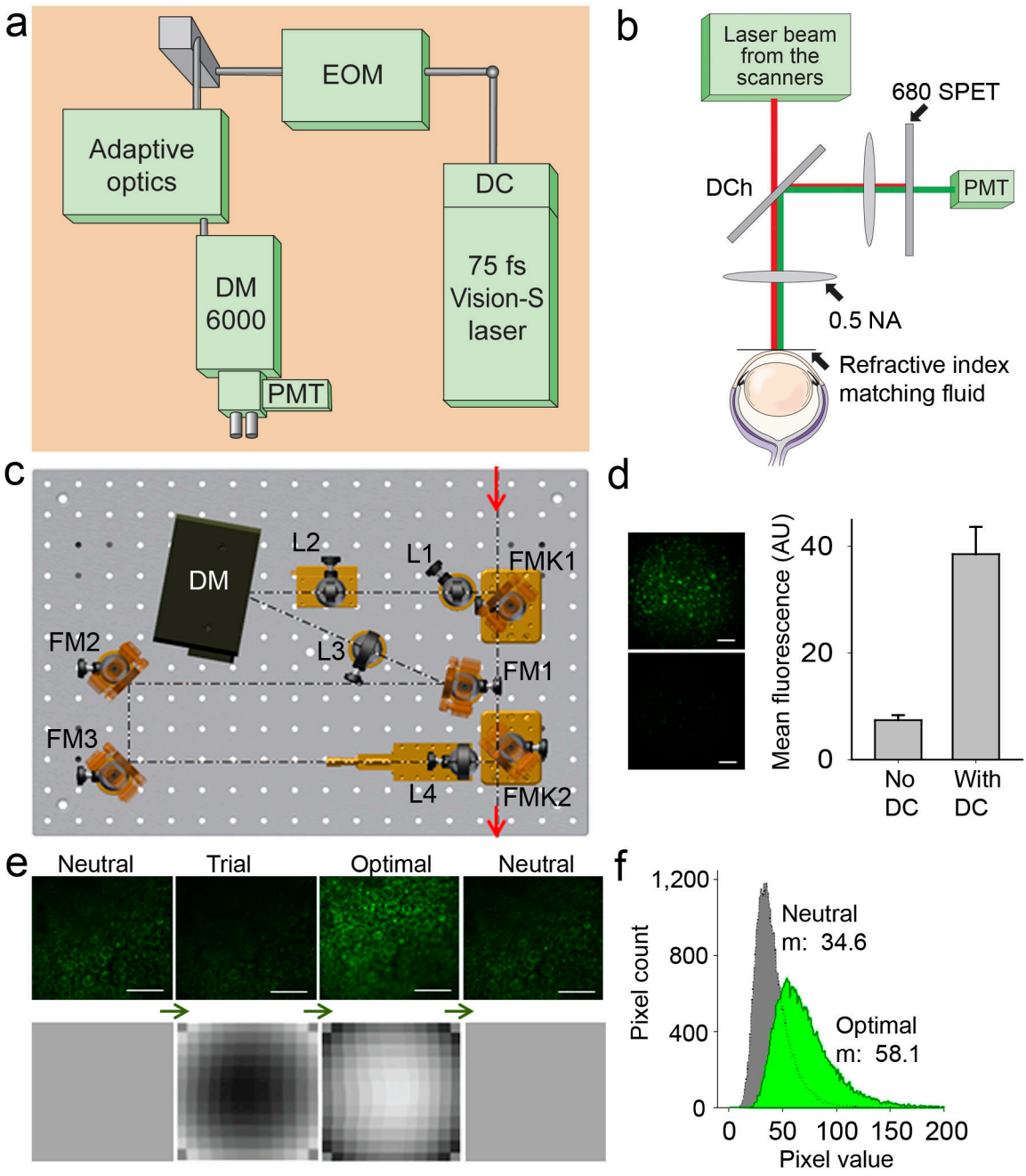

Figure 1.

Two-photon microscopy (TPM) for imaging of mouse retina and RPE. (**a**) TPM system layout. DC stands for group velocity dispersion pre–compensation; EOM - electro–optic modulator; DM6000 - upright microscope; PMT - photomultiplier tube. (**b**) Dichroic mirror (DCh) and barrier filter 680 SPET separate fluorescence and excitation light. (**c**) Layout of the adaptive optics system. FMK1 and FMK2 stand for fold mirrors on kinematic magnetic bases; L1, L2, L3 and L4 - lenses; DM - deformable mirror; FM1, FM2 and FM3 - fold mirrors. (**d**) Left panel, RPE image in an *ex vivo* 1-month-old *Abca4*$^{-/-}$*Rdh8*$^{-/-}$ mouse after exposure to bright light, obtained with (top image) and without (bottom image) DC; right

panel, mean fluorescence measured with and without DC; error bars indicate S.D, n=3. (**e**) Upper row, images of the RPE in an *ex vivo* 3-month-old *Rpe65*$^{-/-}$ mouse obtained during DM optimization: left, at the start of optimization, with DM in the neutral position; right, at the completion of the imaging session; trial represents an image obtained with non-optimal DM settings; optimal, - an image obtained with DM settings that improved image quality. Bottom row pictures the corresponding DM surfaces. (**f**) Quantification of image quality, m stands for mean. Scale bars represent 100 μm.

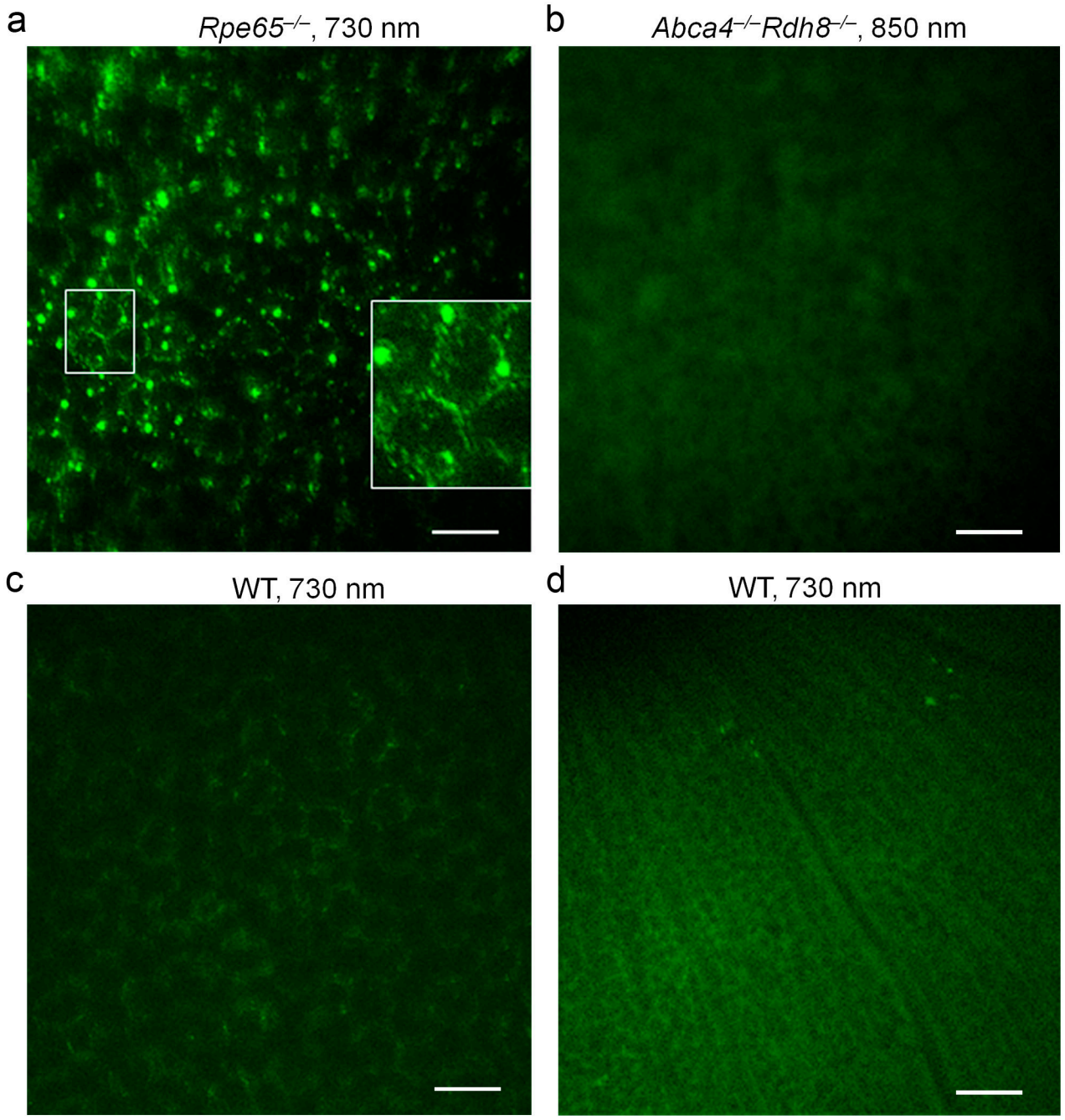

Figure 2.

Two–photon images of *ex vivo* mouse RPE and retina obtained through the mouse eye pupil. Excitation wavelengths and genetic background are listed in each image. (**a**) The RPE in 3-month-old *Rpe65*$^{-/-}$ mouse eye. The inset in the right bottom quarter provides a magnified view of the RPE from the area outlined with a white rectangle. (**b**) The RPE in 6-month-old *Abca4*$^{-/-}$*Rdh8*$^{-/-}$ mouse eye. (**c**) The RPE in 2-month-old WT mouse eye. (**d**) The ganglion cell layer in 2-month-old WT mouse eye. White arrows in **b** and **d** point to the nuclei. Scale bars represent 50 μm in all panels.

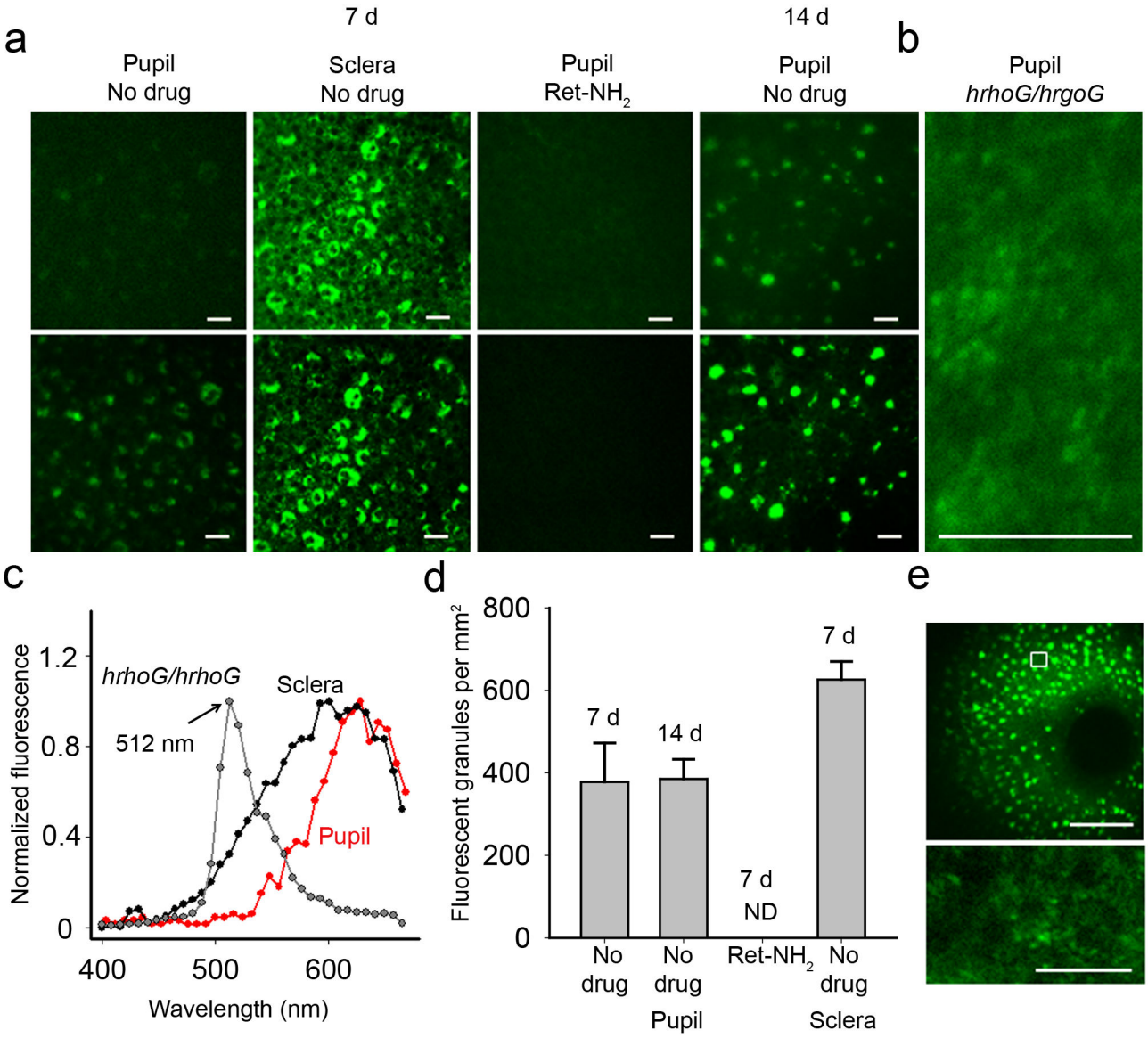

Figure 3.

Use of two-photon imaging for ophthalmic drug screening. (**a**) Ret–NH_2 protects RPE of 1-month-old *Abca4*$^{-/-}$*Rdh8*$^{-/-}$ mouse from bright light induced accumulation of fluorescent granules. Representative *ex vivo* images obtained 7 and 14 days after bright light exposure; images obtained with a 'through the sclera' configuration are included for comparison. Excitation with 730 nm was used for the upper row images whereas 850 nm was employed for the lower row. (**b**) Individual rod photoreceptors expressing rhodopsin-GFP fusion protein are visible in photoreceptor layer of 2-month-old *hrhoG/hrhoG* mice. (**c**) Two-photon excited emission spectra from fluorescent granules in the RPE of *Abca4*$^{-/-}$*Rdh8*$^{-/-}$ mouse obtained through the sclera (black) and pupil (red). Spectrum from photoreceptors in *hrhoG/hrhoG* mice is shown in gray. (**d**) Quantification of Ret–NH_2 impact on accumulation of fluorescent granules in the RPE, based on images as shown in (**a**); ND stands for none detected; error bars indicate S.D., n = 3. (**e**) Lower zoom image of the RPE

in 6-week-old mouse not treated with Ret–NH_2, showing the optic disc is displayed in upper panel. Lower panel shows a magnified view from RPE area outlined with white rectangle in the upper image. Scale bars represent 30 μm in (**a, b**) and lower panel of (**e**) and 220 μm in the upper panel of (**e**).

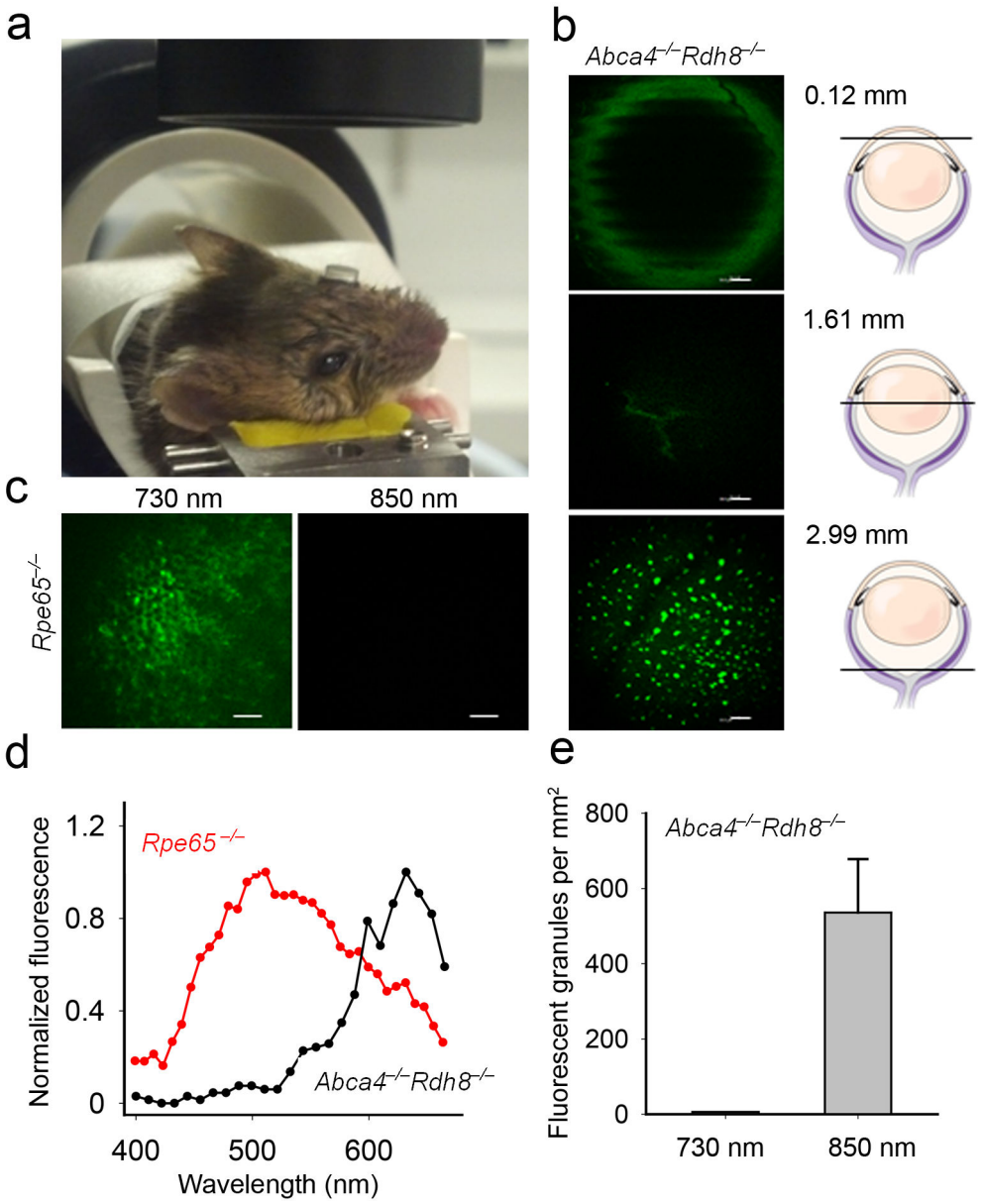

Figure 4.

Set-up for two-photon RPE imaging in living mice. (**a**) During imaging a contact lens covers mouse eye facing the objective. (**b**) Representative images of a pigmented 7-week-old *Abca4*$^{-/-}$*Rdh8*$^{-/-}$ mouse eye obtained *in vivo* with 850 nm excitation 14 days after exposure to bright light, at different depths along Z-axis; a 120 μm section through the cornea, a 1608 μm section showing lens sutures, and a 2987 μm section revealing fluorescent granules in the RPE. (**c**) Images of the RPE in live albino 7-week-old *Rpe65*$^{-/-}$ mice obtained with 730 nm and 850 nm excitation. (**d**) Fluorescence emission spectra from RPE of 7-week-old *Abca4*$^{-/-}$*Rdh8*$^{-/-}$ mice obtained with 850 nm and 7-week-old *Rpe65*$^{-/-}$ mice obtained with 730 nm excitation light *in vivo*. (**e**) Quantification of fluorescent granules. Error bars indicate S.D., n = 3.